Single-nucleus expression analysis characterizes non-enhancing region of recurrent high-grade glioma

Kunal S. Patel[1]*, Kaleab K. Tessema[2]*, Riki Kawaguchi[3], Alvaro G. Alvarado[2], Sree Deepthi Muthukrishnan[2], Akifumi Hagiwara[4], Vivek Swarup[5], Linda M. Liau[1], Anthony Wang[1], William Yong[6], Daniel H. Geschwind[3], Ichiro Nakano[7], Steven A. Goldman[8,9], Richard Everson[1#], Benjamin M. Ellingson[1,4#], Harley I. Kornblum[2,10#]

[1]Department of Neurosurgery, David Geffen School of Medicine at UCLA, Los Angeles, CA

[2]The Intellectual and Developmental Disabilities Research Center and Department of Psychiatry and Biobehavioral Sciences, David Geffen School of Medicine at UCLA, Los Angeles, CA

[3]Department of Neurology, David Geffen School of Medicine at UCLA, Los Angeles, CA

[4]UCLA Brain Tumor Imaging Laboratory (BTIL), Department of Radiological Sciences, David Geffen School of Medicine at UCLA, Los Angeles, CA

[5]Department of Neurobiology and Behavior, UCI School of Biological Sciences, Irvine, CA

[6]Department of Pathology, David Geffen School of Medicine at UCLA, Los Angeles, CA

[7]Department of Neurosurgery, Hokuto Social Medical Corporation, Hokuto Hospital, Hokuto, Japan

[8]Center for Translational Neuromedicine, University of Rochester Medical Center, Rochester, NY

[9]Center for Translational Neuromedicine, University of Copenhagen Faculty of Health and Medical Sciences, Copenhagen, Denmark

[10]Departments of Pediatrics and Molecular and Medical Pharmacology, David Geffen School of Medicine at UCLA, Los Angeles, CA

*These authors contributed equally to this work

[#]These authors jointly supervised this work

Conflicts of interest: The authors have declared that no conflict of interest exists.

Corresponding Authors

Harley Kornblum, M.D., Ph.D.

NRB Room 375D, UCLA

635 Charles E. Young Drive South

Los Angeles, CA 90095

hkornblum@mednet.ucla.edu

310-794-7866

Abstract

Non-enhancing (NE) infiltrating tumor cells beyond the contrast-enhancing (CE) bulk of tumor are potential propagators of recurrence after gross total resection of high-grade glioma. We leveraged single-nucleus RNA-sequencing to compare prospectively identified biopsy specimens from CE and NE regions. Recurrent gliomas recapitulate the previously reported glioma cellular states of primary gliomas. Tumor cells in NE regions are enriched in oligodendrocyte progenitor cell-like and neural progenitor cell-like cellular states, while CE regions are enriched for astrocyte-like and mesenchymal-like states. These NE glioma cells have similar copy number alterations and proportions of proliferative and putative glioma stem cells relative to CE regions. Tumor cells in NE regions exhibit upregulation of genes previously associated with lower grade gliomas. Cell-, gene-, and pathway-level analyses of the tumor microenvironment in the NE region reveal relative downregulation of tumor-mediated neovascularization and cell-mediated immune response, but increased glioma-to-neuron interactions. This comprehensive analysis illustrates differing tumor and non-tumor landscapes of CE and NE regions in high-grade gliomas, highlighting the NE region as an area harboring likely initiators of recurrence in a pro-tumor microenvironment and identifying possible targets for future design of NE-specific adjuvant therapy.

Introduction

The intervention that contributes most to overall survival in adult glioma remains surgical removal of tumors (1, 2). The current surgical standard of care is imaging-based resection of the contrast-enhancing (CE) region as depicted by gadolinium contrast-enhanced T1-weighted magnetic resonance imaging (MRI) (3), where increased extent of resection (4) and lower post-surgical residual enhancing disease (5) have been shown to be correlated with improved survival. However, despite total resection of the CE region, high-grade gliomas invariably recur, and this most commonly occurs at the edge of the resection cavity (6).

Treatment options for recurrent malignant glioma include repeat resection with adjuvant molecular therapy (7–9) and/or immunotherapy (10). Given the modest efficacy in randomized trials, further study into treatment for recurrent glioma is needed. Strategies for molecularly targeted therapy for recurrent glioma have largely been developed by studying bulk RNA or protein expression from cell lines or clinical surgical specimens, which, as described above, generally derive from the CE portion of the tumor. This strategy 1) fails to account for cellular heterogeneity and 2) ignores the true targets of adjuvant therapy for glioma: the residual cells beyond the CE region that are not resected. While more recent studies have utilized single-cell sequencing to study intratumoral heterogeneity (11–18), they have largely focused on single samples from CE regions, yielding limited insight about infiltrating cells beyond the CE region and their clinical relevance. Furthermore, in addition to understanding infiltrating tumor cells, it is important to understand the non-tumor microenvironment along with tumor-microenvironment interactions in regards to immune response, vasculature, and normal nervous system function (10).

In this study, we prospectively sample CE regions and tissue beyond the enhancing edge (non-enhancing, "NE") from seven recurrent gliomas: four grade 4 IDH-wildtype glioblastomas, one grade 4 IDH-mutant astrocytoma, one grade 3 IDH-mutant oligodendroglioma, and one grade 2 IDH-mutant oligodendroglioma. We couple intraoperative neuronavigation-guided targeting of biopsy specimens with single-nucleus RNA-sequencing (snRNA-seq) to comprehensively characterize region-specific cellular and molecular features. Our experimental design differs from previous single-cell analyses in glioma in that we leverage prospectively determined positional data to model the spatial landscape of cell populations within CE and NE regions, producing an improved (19) yield of single-cell data from NE regions of tumor. We perform a comprehensive single-cell characterization of the NE region to assess tumor cell burden, composition of tumor and non-tumor cells, molecular features of tumor and non-

tumor cells, and tumor-microenvironment interactions. These data provide an important description of the biological landscape of infiltrating tumor cells and identify potential targets for improved post-operative adjuvant therapy.

Results

Analysis of human recurrent gliomas using single-nucleus RNA sequencing

We prospectively identified biopsy targets using pre-operative MRI in 7 patients undergoing surgery for recurrent glioma (Table 1). We chose recurrent glioma given its clinical burden and limited single-cell analysis of recurrent glioma relative to primary glioma (13). Each patient had a single previous resection with adjuvant temozolomide and radiation therapy only. We selected two biopsy targets from the contrast-enhancing (CE) region of each tumor and one from the non-enhancing (NE) region, located 5-20mm from the CE edge (Fig. 1A). Clinical pathology and fluorescence in situ hybridization identified six high-grade gliomas (four grade 4 IDH-wildtype glioblastomas, one grade 4 IDH-mutant astrocytoma, one grade 3 IDH-mutant and 1p/19q co-deleted oligodendroglioma) and one low-grade glioma (grade 2 IDH-mutant and 1p/19q co-deleted oligodendroglioma) (Table 1). We refer to these tumors as Gr4-GBM, Gr4-AST, Gr3-ODG, and Gr2-ODG, respectively (20). To analyze these tumors, we performed single-nucleus RNA-sequencing (snRNA-seq) of all biopsy specimens (Fig. 1B), yielding 32,914 individual transcriptomes that passed rigorous quality control and were included in subsequent analyses (Table 1, Fig. 1C, Fig. S1A-B).

Characterization of malignant cells in recurrent glioma highlights intra- and inter-tumoral heterogeneity

To study malignant cell heterogeneity, we first developed an approach that improves upon previously reported strategies for malignant cell identification (13, 16, 21). We combined marker expression, hierarchical relationships across unbiased clusters, and an iterative sequence of single-nucleus copy number alteration (CNA) inference analyses to mitigate the effects of classification issues related to inherent clustering flaws or unclear CNA profiles (Supp. Methods). Malignant cells (Fig. 1D, Fig. S1C-D) were then stratified into four cellular states—astrocyte-like (AC-like), mesenchymal-like (MES-like), neural progenitor cell-like (NPC-like), and oligodendrocyte precursor cell-like (OPC-like)—and cycling vs. non-cycling using the module scoring system reported by Neftel et. al (13) (Fig. 2A-B, Fig. S2A-C). Similar to the intratumoral heterogeneity seen in primary gliomas (11–13, 21), all four cellular states were identified in our dataset, and there was significant intertumoral heterogeneity in cellular state composition (Fig. 2C; ANOVA FDR<0.05 for all states). Despite the limited number of non-GBM samples precluding formal statistical assessment, OPC-like and MES-like proportions appeared to vary with tumor

pathological designation. OPC-like proportion was highest in Gr2-ODG (74.7%), followed by Gr3-ODG (55.4%), Gr4-AST (44.3%), and Gr4-GBM (20.7%). In contrast, MES-like proportion was highest in Gr4-GBM (35.7%), followed by Gr4-AST (9.9%), Gr3- ODG (0.15%), and Gr2-ODG (0.11%). IDH-wildtype tumors (Gr4-GBMs) trended towards lower OPC-like proportions (20.7% vs. 58.1%, unpaired t-test $p = 0.063$) and higher MES-like proportions (35.4% vs. 3.4%, unpaired t-test $p=0.21$) than IDH-mutant tumors (Gr4-AST, Gr3-ODG, and Gr2-ODG). AC-like and NPC-like proportions varied among tumors but did not clearly relate to diagnosis. There was also significant heterogeneity in the cycling fraction within malignant cells (Fig. 2C; ANOVA FDR<0.05), with a higher proportion in Gr4-GBM versus the remaining tumors (8.5% versus 1.6%; unpaired t-test $p=0.115$). While all four cellular states were observed to have cycling cells, NPC-/OPC-like cells had the highest cell cycling fractions when present (7.7% vs. 2.2% in MES-/AC-like cells, unpaired t-test $p=0.018$) and were the only cycling cells in the two oligodendrogliomas (Fig. 2D). We also quantified cellular heterogeneity using an unbiased machine learning algorithm that measures "separability" of cellular populations based on global transcriptomic differences (22). As with primary gliomas, there was greater intertumoral heterogeneity (i.e., separability of patient identity within each cellular state) than intratumoral heterogeneity (i.e., separability of cellular state within each tumor) (Fig. 2E; $p<0.001$, Welch's t-test).

Significant tumor burden and altered malignant cell composition in the NE regions of high-grade gliomas

We used MRI-based positional information to compare the contrast-enhancing (CE) and T2 hyperintense non-enhancing (NE) regions of three Gr4-GBMs, Gr4-AST, and Gr3-ODG (Gr4-GBM-4 only had CE cells that passed QC and Gr2-ODG was a non-enhancing tumor) (Fig. 3A). We first assessed tumor burden in the NE region by quantifying malignant cell proportions, revealing a notable malignant cell burden present in the NE region in all patients (15.3-60.6% of NE cells; NE / CE malignant cell ratio of 0.58-1.13; Fig. 3B, Fig. S3A-B). Given that malignant cells comprised a notable proportion of the NE regions, we sought to model the spatial extent of tumor burden on MR imaging. Using tumor cell quantity from three locations in two tumors (Gr4-GBM-1 and Gr4-AST), we applied a quadratic model (see Methods) to extrapolate the distance from the center of the tumor to where the tumor burden would approach 0 (Fig. 3C). This model predicted tumor cell presence 4.94 cm and 2.31 cm, respectively, from the center of the tumor, and a spheroid with this radius was constructed and overlaid on the corresponding pre-operative MR image (Fig. 3D). The predicted tumor edge was beyond the CE region by 2.45 cm in Gr4-GBM-1 and 0.34 cm in Gr4-AST. While the invasion and growth patterns of glioma are complex, with cases

of multifocal and distant lesions (23), our data suggest a consistent presence of marked and potentially clinically significant tumor burden immediately surrounding the CE bulk.

We then examined malignant cell subpopulations across regions and noted significant heterogeneity both in terms of cluster proportions (Fig. S3C) and cellular state composition (Fig. 3E). In line with previous studies (24–26), NE regions of all Gr4-GBMs harbored a higher NPC-like proportion (mean +14%, paired t-test p=0.03) and lower MES-like proportion (mean -15.0%, paired t-test p=0.12), while AC- and OPC-like proportions were not consistently different. There was a cycling fraction in the NE regions of all tumors (Fig. 3F), with no significant difference between regions (mean +0.51% in NE, paired t-test p=0.792). To further characterize tumor cell cycling via immunohistochemistry, we obtained image-guided biopsies from an additional cohort of 17 patients with high-grade glioma and analyzed a total of 22 tissue specimens from NE regions and 24 from CE regions (Table S1). Quantification of Ki-67 staining showed a wide distribution in both regions, including several NE samples with high Ki-67 positivity, but no significant difference between regions (p=0.0957, unpaired t-test; Fig. 3G). We also analyzed paired samples from five patients with both regions sampled during the same procedure, and while there was a trend towards a higher fraction of Ki-67-positive cells in the NE region of each tumor, the effect did not reach statistical significance (p=0.0875, paired t-test; Fig. 3H-I). We then asked whether cycling proportion could be a useful prognostic tool in assessing tumor burden in the NE region, since the current standard of care does not include excision and characterization of this region. We found that the cycling proportion of malignant cells in CE (but not NE) was predictive of tumor burden in NE (p<0.001, Spearman's rho=1). Finally, we noted regional differences in cycling tendencies of individual cellular states (Fig. S3D). There were cycling OPC-like and NPC-like cells in NE regions in all tumors. Only Gr4-GBM-3 had cycling AC-like cells (1.7%) in the NE region. In all samples, the vast majority (>85%) of cycling malignant cells in the NE region were OPC- or NPC-like cells (Fig. S3E). Together, these data indicate that there are ample numbers of proliferating tumor cells in the NE region and implicate NPC-like and OPC-like cellular states as the cellular majority and major contributors to proliferation in the NE region.

Gene expression and pathway enrichment profiles in malignant cells from NE regions

To investigate regional heterogeneity in malignant cell transcriptomes, we identified differentially expressed genes (DEGs) between regions. In the NE regions, there were between 78-1005 upregulated and 43-2356 downregulated

genes in each tumor (Fig. 4A-B, Fig. S4A, Table S2). DEGs were also identified within each cellular state, both conserved across tumors and within each tumor (Fig. 4A, Fig. S4B, Table S2). Top NE-enriched DEGs (change > 25% and adjusted $p < 1e^{-10}$) included genes associated with neuronal/synaptic function (e.g., *TNR, NRXN1, ANKS1B, CADM2, IL1RAPL, PAK3, PLCL1, ERC2, SCN3A, KCN3*), genes upregulated in lower grade gliomas (e.g., *TNR, GALANT13, TMEFF2, PAK3, SPOCK1*) (27–31), and genes associated with immune-cold phenotypes (e.g., *NRXN1*) (32). Top CE-enriched DEGs included genes associated with metabolism (e.g., *ABCA1* (33), *NAMPT* (34)), proliferation/invasion (e.g., *CD44* (35), *SPP1* (36), *IGFBP7, IGFBP5* (37), *RYR3* (38), *TNC* (39)), and angiogenesis (e.g., *VEGFA, IGFBP7* (40), *TNC*). To further determine functional implications of NE-specific transcriptional patterns, DEGs were then used as input for gene set enrichment analysis (GSEA) (41) with a combination of databases: Gene Ontology Biological Pathways, Canonical Pathways, Oncogenic Pathways, and Transcription Factor Targets (42). There was a wide range of differential pathway activation in NE across patients compared to CE: grade 4 tumors had 483-1143 differentially enriched pathways, while Gr3-ODG had only 56 (Table S3). Conserved DEGs in malignant cells across tumors pointed to 686 significantly differentially activated pathways in NE vs. CE (Benjamini-Hochberg adjusted $p<0.05$) (Table S3). The top 20 NE-enriched pathways (normalized enrichment score > 2.0) were all related to neuronal/synaptic function, while the top 20 CE-enriched pathways included interferon-gamma signaling, growth factors, vasculature development, and extracellular matrix regulation.

We then examined differential pathway regulation in NE vs. CE within each malignant cellular state (Fig. 4C, Table S3). GSEA using conserved DEGs across tumors revealed that AC-like and MES-like cells had the most differentially activated pathways (103 and 46, respectively). AC-like cells in NE regions had upregulated neuron-, synapse-, and cell-cell interaction-related pathways and downregulated antigen presentation, signaling via the oncogenic transcription factor CRX, immune response, and translation elongation. MES-like cells in NE exhibited upregulation of proliferation and downregulation of translation, Slit-Robo signaling (promotes angiogenesis) (43–46) (52), regulation of micro-vasculature density, and VEGF-induced migration/permeability. NPC-like cells exhibited 32 differentially activated pathways; in NE, PI3K was upregulated and neuron recognition, p53, and cell-cell adhesion were downregulated. OPC-like cells in NE only showed upregulation of the node of Ranvier cellular compartment. In cycling cells, DNA replication was upregulated in NE and FOXJ2 signaling and factor X were downregulated.

To complement the gene- and pathway-level comparisons, we comprehensively evaluated the degree of cellular heterogeneity by leveraging Augur (22) again to measure "separability" of cell populations, or how well an unbiased machine learning algorithm can learn to accurately predict a cell's identity (e.g., patient, region, or cellular state) given its transcriptome. Measuring regional separability, or accuracy in predicting whether a cell came from NE or CE sample, of each cellular state revealed significant heterogeneity across tumors: the most regionally separable cells were AC-like and/or MES-like in Gr4-GBMs and OPC-like and NPC-like in Gr4-AST and Gr3-ODG. To assess whether regional phenotypes converge across patients or cellular states, we then asked whether there were statistically significant differences in intertumoral (separability of patient identities) or intratumoral (separability of cellular states) heterogeneity in NE compared to CE and found that there was significantly more intertumoral heterogeneity within AC-like and MES-like populations in CE compared to NE (classification accuracy = 0.839 and 0.837 in CE, 0.765 and 0.749 in NE, respectively; $p<0.01$ for both, permutation test, BH-corrected), suggesting these populations are more similar across patients in the NE regions; on the other hand, intertumoral heterogeneity in NPC-/OPC-like cells was similar across regions (Fig. 4D). There were no significant regional differences in heterogeneity within cycling and non-cycling compartments or in intratumoral heterogeneity of cellular states (Fig. S4C). Taken together, our gene-, pathway-, and population-level analyses show significant differences between malignant cells in the NE and CE regions and that these differences are driven by specific glioma cellular states.

Regional comparison of putative glioma stem cells and copy number subclones

Glioma initiation, progression, invasion, and recurrence may be driven by specific cell populations that are potentially present in residual NE regions. These cells may have certain stem-like properties or specific copy number alterations contributing to their phenotypes (47). While putative glioma stem cells (GSCs) have been well studied, there is no universally accepted genomic or transcriptomic definition. To evaluate regional differences in GSC populations, we used nine previously studied "GSC" (for simplicity) gene signatures (12, 16, 21, 47–51) (Table S4) and identified putative GSCs in our dataset (Fig. 4E, Fig. S4D). There was significant heterogeneity in GSC fraction (mean 0%-38%). Interestingly, three studies appeared to highlight similar GSC populations: outer radial-glia like cells from Bhaduri et al. (48), quiescent GSCs from Xie et al. (49), and mesenchymal GSCs from Wang et al. (16). There was no clear difference in proportion of GSC populations between IDH wild-type (Gr4-GBMs) and IDH-mutant (Gr4-AST and Gr3-ODG) tumors ($p > 0.05$ each). Comparing GSC proportion in CE vs. NE yielded no consistent difference ($p > 0.05$ each). Importantly, all definitions revealed putative GSCs in NE

regions. We next analyzed the cellular state composition of each GSC population and found a high degree of variability across definitions (Fig. S4E). AC- and MES-like cells comprised the majority of outer radial glia-like cells (48), quiescent GSCs (49), and mesenchymal GSCs (16). On the other hand, OPC- and NPC-like cells comprised the majority of proneural (16) and transcription factor-based (50) GSCs. We next evaluated regional variability in copy number alteration-based subclone composition (Fig. S4F-G). Number of identified subclones were 3-7 for Gr4-GBMs, 2 for Gr4-AST, and 4 for Gr3-ODG. While there was heterogeneity in subclone proportion in CE and NE in all tumors, all subclones existed in both the CE and NE regions. Overall, investigating these glioma populations with previously established roles in tumor initiation, propagation, invasion, and recurrence implicates residual NE regions as harboring critical populations that may serve as targets of adjuvant therapy.

Composition and molecular features of non-malignant cell populations in NE regions

We next focused on regional differences in the tumor microenvironment. Using marker expression patterns and hierarchical clustering, we annotated non-malignant clusters as astrocytes, oligodendrocytes, excitatory neurons, interneurons, endothelial cells, T cells, microglia, and tumor-associated macrophages (Fig. 5A, Fig. S5A-B). We first examined cell type composition and noted that oligodendrocytes were the most represented cell type in all tumors except for Gr4-GBM-1, which had a neuronal majority (likely due to the biopsy sites' proximity to gray matter rather than white matter). This highlights the invasive nature of glioma, with malignant cells integrating into non-pathological brain tissue. Comparing composition across regions revealed lower T cell proportions in NE for all tumors (mean 0.56% vs 1.94%, paired t-test p=0.14; Fig. 5B). Consistent with previous reports (19), the macrophage:microglia ratio was higher in the CE regions of all tumors except Gr4-GBM-2. There were no clear regional patterns in other cell type proportions.

We examined global and cell type-specific regional transcriptomic differences in non-malignant cells by identifying differentially expressed genes (DEGs) in NE vs. CE in the integrated dataset (Fig. 5C-D, Fig. S5C, Table S5). Excitatory neurons and oligodendrocytes had the highest DEG proportion (66% and 54%, respectively) of all tested genes, which were those expressed in at least 5% of cells. In oligodendrocytes, heat shock proteins (e.g., *HSPA1A, HSPH1)* and the metabolic gene *ENOX2* were NE-enriched, while *VEGFA* was CE-enriched. In neurons, genes associated with hypoxic conditions (e.g., *NGB*) and increased metabolism (e.g., *MT-ATP6, MT-CO1, MT-CO2, MT-CYB*) were NE-enriched, while genes related to cell adhesion (e.g., *CADM2, LAMA2, CDH18*) and neuronal

function (e.g., *DLG2, NRG3, CSMD1, PARK2*) were CE-enriched. In microglia, heat shock protein genes (e.g., *HSPA1B, HSP90AA1, HSPH1*) were NE-enriched, and a gene associated with monocyte-to-macrophage differentiation (*CPM*) was CE-enriched. In macrophages, genes associated with interaction and reorganization of the extracellular matrix (e.g., *TNS1, VIM, TRIO*) were CE-enriched. Lastly, genes involved in blood-brain barrier (e.g., *CLDN11, PDGFRb*) were NE-enriched in non-tumor cells.

We also assessed regional enrichment of functional pathways in non-malignant cells using GSEA, which revealed a large degree of heterogeneous pathway activation (Fig. 5E, Table S6). In oligodendrocytes, we observed upregulated HSF1 activity and downregulated Slit/Robo signaling (43–46)(52) in NE. In neurons, we observed upregulation of oxidative phosphorylation and translation and downregulation of endothelin and neuron/synapse terms in NE. Evaluation of microglia demonstrated upregulation in metabolism and downregulation in immune function in NE, with macrophages interestingly exhibiting the opposite pattern. These cell-, gene-, and pathway- level analyses identify unique features of the non-tumor microenvironment in NE regions, highlighted by decreased T cell fractions, possible region-specific myeloid phenotypes, and markers of cellular stress (e.g., HSF1) in multiple cell types. Furthermore, these data suggest altered regulation of vascular integrity in NE regions, which may explain the limitation of gadolinium leakage from affected blood vessels and therefore lack of contrast enhancement in this region (53).

Cell-cell communication networks in the NE region exhibit differential functional wiring and information flow

Crosstalk between malignant cells and normal cells is a hallmark feature of cancer and is critical to tumor growth, invasion, and recurrence (54–57) .To analyze cell-cell interaction (CCI) networks, we utilized CellChat (58), which uses a comprehensive database of ligand-receptor interactions (Fig. S6A) and performs quantitative inference and analysis of intercellular communication via network analysis, pattern recognition, manifold learning, and quantitative contrast approaches. We first built a CCI atlas for each tumor to examine general principles of cellular communication. The five high-grade gliomas that yielded both CE and NE cells were analyzed individually, with malignant and non-malignant cells combined. We identified between 112-150 putatively active CCI pathways in each tumor (Fig. S6B, Table S7) out of 223 total pathways in the database. A total of 160 unique pathways were identified; 96 were detected in all tumors and 13 were specific to one tumor. The putative connectome of each tumor had a rich network structure that involved both paracrine and autocrine communication among cell types (Fig. 6A-

B). We performed differential analysis to identify shared and patient-specific CCI differences between NE and CE. For each tumor, the NE and CE regions were analyzed separately and compared with each other using only the cell types present in both regions. While the number of ligand:receptor interactions identified was lower in NE for four of the five tumors (Fig. S6C-E), communication strength (i.e., probability) was higher in NE for four of the five tumors (Fig. 6D). Assessing individual cell types identified several patterns. The cell types with the largest regional difference in outgoing communication were also the cell types with the largest regional difference in incoming communication, suggesting coordinated regional variation in both ligands and receptors in those cell types (astrocytes in Gr4-GBM-1; oligodendrocytes in Gr4-GBM-2; neurons in Gr4-GBM-3; endothelial cells and astrocytes in Gr4-AST and Gr3-ODG). The most upregulated glioma-to-normal cell interactions in NE relative to CE were glioma:oligodendrocyte and glioma:neuron in Gr4-GBMs, glioma:astrocytes in Gr4-AST, and glioma:oligodendrocytes in Gr3-ODG (Fig. 6C, E). In Gr3-ODG and Gr4-AST, all CE-enriched interactions involved either neurons or astrocytes, whereas CE-enriched interactions in Gr4-GBMs were more diverse and include pairs of glioma, immune, and endothelial cells. Multiple endothelial cell interactions (endothelial:T cell, endothelial:endothelial, T cell:endothelial, and oligodendrocyte:endothelial) were NE-enriched or unchanged across tumors.

To identify specific CCI pathways driving regional heterogeneity, we compared NE and CE using two pathway-level metrics: 1) functional wiring (major source/target cell types and directionality of communication) and 2) information flow (overall signaling strength of each communication pathway). For each tumor, we identified the most functionally dissimilar signaling pathways in NE vs. CE via joint manifold learning and classification of the inferred communication networks based on their functional similarity (Fig. S7A-C, Table S7). This revealed SEMA7 (migration) (59), Activin (proliferation) (60), and BAFF (B-cell activation) (61) as the most conserved pathways, each of which was differentially wired in NE vs. CE in four tumors (Fig. 7A). In terms of differential information flow between NE and CE, 50-77 pathways were identified as significantly different in each tumor (Fig. S8A-C, Table S7). CD40 (62) was the only differentially activated pathway between NE and CE in all tumors (Fig. 7B). Separating communication pathways into CE- and NE-enriched revealed that CD40 signaling was CE-enriched in all tumors, NT and LIGHT/TNFSF14 (63) were CE-enriched in four tumors, and PVR/CD155 (invasion/infiltration) (64) and MAG (myelin interaction) were NE-enriched in four tumors (Fig. 7C-D). Additional conserved CE-enriched pathways included immune (IL1, IL10, IL4, TIGIT) and endothelial (CDH5) mediators, and

conserved NE-enriched pathways included heparin binding growth factor pathways (MK, PTN) (65) and microglial attraction (GDNF) (66). Together, these findings highlight global and cell type-specific differences in the cellular communication landscape of NE regions.

Discussion

In this study, we leveraged single-nucleus RNA-sequencing and MRI-guided biopsy target selection to dissect spatial phenotypes in recurrent glioma. While prior studies have characterized cells in both NE and CE regions (19, 67), our approach has the advantage of being able to capture sufficient numbers of cells from each region to ascertain regional differences.

Our study takes advantage of two unique characteristics: 1) inclusion of multiple WHO designations of high-grade glioma (20) and 2) examination of recurrent glioma. We compared glioma subtypes using the cellular state model described by Neftel et al. (13), who identified gene networks that consistently drive intratumoral heterogeneity in a large cohort of patients. We found that the proportions of glioma cellular states appeared to be related to pathological diagnosis, as AC- and MES-like compartments were expanded in tumors with higher WHO grade. These differences parallel 1) imaging findings (presence of contrast enhancement and necrosis), 2) pathologic differences (neovascularization, invasion, and necrosis), and 3) survival differences among gliomas. The Gr4-AST subtype fit within this context, with cellular state proportions and clinical outcomes falling between Gr3-ODG and Gr4-GBM. We hypothesize that the imaging, pathological, and clinical differences in recurrent glioma may be driven by biological heterogeneity due to different cellular state compositions.

We exclusively studied recurrent tumors due to the relative lack of information, including regional differences in these tumors, allowing us to compare what is known about the more extensively studied primary glioma. We show that in recurrent high-grade gliomas, tumor biology is similar to primary gliomas (13, 14, 21), including the presence of all four malignant cellular states (13). In addition, the cycling tendencies of the different cellular states are conserved in recurrent tumors relative to data from primary glioma (13, 15). Recurrent glioma may therefore be recapitulating a tumor that is similar to its primary counterpart. In fact, it may be that “recurrent glioma” is a misnomer; given that the surgical standard of care is maximal safe resection of the CE region of tumor (1), “recurrent glioma” may actually be the natural progression of residual glioma cells left in the infiltrative NE regions surrounding the resection cavity.

With this in mind, we focused on characterizing these infiltrating NE regions on a single-cell level by taking MRI-guided samples of these areas during surgery. We confirmed there was significant tumor burden beyond the CE region in all recurrent high-grade gliomas. Our model predicted that cells may exist multiple centimeters beyond the CE edge, potentially occurring in a portion of FLAIR hyperintensity surrounding the tumor. NE regions had similar levels of cycling cells, putative GSCs, and copy number subclones as CE regions, suggesting these residual areas likely harbor propagators of progression and recurrence after gross total resection of CE tumor.

We use cell-, gene-, pathway-, and interactome- level analyses to characterize both infiltrating tumor and microenvironment in the NE region. We found regional differences in cellular state composition that are consistent with previous findings in primary glioma: Minata et al. (26) identified higher MES-like cells in CE regions and higher NPC-like cells in NE regions. We noted that NPC-/OPC-like cells were more abundant in both the low-grade, non-enhancing tumor and in the NE regions of high-grade tumors. Differential expression analysis showed upregulation of genes associated with lower grade tumors and downregulation of genes associated with proliferation/invasion in NE regions. Furthermore, the cycling cells of NE regions were almost exclusively OPC-like and NPC-like. These data suggest potential relationships between cellular states and MRI findings in that NPC-/OPC-like cells correlate with non-enhancing characteristics and lower grade biology, while MES-/AC-like cells correlate with contrast-enhancing characteristics and higher-grade biology. With this in mind, we hypothesize that while there are many similar characteristics between cells in the NE and CE, some of their distinct properties may guide future potential treatments targeting these NE cells.

Several distinguishing features of the NE regions converged on vasculature biology. Malignant cells in the NE region had significant downregulation of genes associated with angiogenesis as well as decreased activity of vascular pathways. There were extremely small numbers of non-transformed endothelial cells in the NE region, and they had relative upregulation of genes associated with the blood-brain-barrier. Interestingly, non-tumor, non-endothelial cells in the NE region had evidence of hypoxic stress, with upregulation of *NGB* and heat shock proteins and increased HSF1 pathway activity. Lastly, we see upregulation of the CDH5 pathway, involved in GSC-to-endothelial transition (68), in CE. We hypothesize that NE regions may contain infiltrating, proliferating tumor cells with reduced tumor-mediated microvascular proliferation. In turn, without the VEGF-mediated aberrant tumor vessels and compromise of the blood brain barrier, there is no leakage of gadolinium during MRI and therefore no

contrast enhancement in this region. We postulate that under hypoxic stress, there would ultimately be relative transition to neovascular programs in the NE region and, therefore, transition to CE tumor. We suggest that modulation of non-tumor vasculature may be a mechanism for improved drug delivery to malignant cells in NE regions.

We also identified regional heterogeneity in the immune microenvironment of recurrent glioma. We found that NE regions harbored lower T cell proportions than CE regions. A previous study comparing core and edge regions in primary glioma (19) found that macrophage:microglia ratio was decreased in edge regions, which our findings also reflected. While macrophages and microglia share many similar properties, we do not know whether regional differences reflect relative differences in their ability to tolerate different microenvironments or whether they represent truly different functions. Furthermore, identifying differences in cell-cell communication between NE and CE regions revealed immune function as a common theme, with significant depletion of tumor necrosis factor-related pathways (e.g., CD40, LIGHT, TIGIT) in NE. The only differentially wired signaling pathway shared among the top hits across tumors was CD40, which was depleted in NE. The CD40 pathway in glioma is a well-studied TNF-mediated pathway that leads to immune stimulation (62, 69, 70) and is correlated with increased survival (70). The relative downregulation of this pathway in NE regions, along with the enrichment of several cell-mediated immunity pathways (e.g., IL1, IL4, IL10) in CE regions implicates the NE region as an immune-cold environment with a hampered immune response to infiltrating tumor cells. We hypothesize that directing an advanced immune response to OPC-like and NPC-like cells in the NE, potentially through CD40 agonism (69), may serve as a therapeutic strategy for suppression of progression after standard of care therapy.

Lastly, we observed regional heterogeneity in communication between glioma cells and non-malignant oligodendrocytes and neurons. NE tumor cells were enriched in genes associated with neuronal/synaptic function. NE regions had stronger glioma-to-neuron and glioma-to-oligodendrocyte signaling. Interactions between infiltrating glioma cells and neurons have been observed (57), suggesting glioma can infiltrate into areas of brain that are still functional. Overall, the NE microenvironment is more similar to normal stroma than the CE region, with decreased immune response, decreased abnormal microvasculature, and increased communication with normal cells. This suggests neuronal circuits may retain function despite infiltration of tumor cells, limiting surgical removal of these cells without sacrificing intact neuronal connections.

Taken together, this study presents a thorough quantification and molecular characterization of both malignant and non-malignant cell populations and their putative functional roles in the NE region of recurrent gliomas. These findings have significant clinical implications. First, the presence of significant tumor burden with actively cycling cells multiple centimeters from the CE edge suggests that resection of the NE region--when not involving eloquent areas, given the potential maintenance of neuronal function in infiltrative areas--may improve outcomes. These regions are often not addressed by surgery (with standard of care being maximal safe resection of CE regions) or adjuvant radiotherapy (with standard of care being radiation to resection cavity with a 2cm margin). Second, considering the inability to resect entire NE regions in many cases due to functional eloquence, these residual NE cells are likely the culprits of recurrence and therefore should be targeted by adjuvant therapy. The presence of cell-, gene-, pathway-, and interactome- level differences in the NE region compared to CE suggests that improvements in adjuvant therapy should be driven by investigation of NE tissue rather than the bulk of the tumor, as is current standard in glioma studies.

Our study has several limitations. Due to the limited number of tumors in each pathological designation, we cannot confidently draw statistical conclusions between types of tumors. Furthermore, the specimens from the NE region in each tumor were limited to a single site given the need to limit sampling of potential non-pathologic neural tissue, leaving open the possibility that different portions of the NE regions behave differently. Lastly, while studying recurrent gliomas allowed comprehensive characterization and comparison with previous findings in primary gliomas, certain conclusions are limited in their generalizability to primary tumors.

Regarding potential strategies to target the NE region, we point to specific malignant populations. The bulk of NE regions consist of NPC-/OPC-like cells, and these cells are the bulk of cycling cells. These cells may continue to interact with normal neurons and oligodendrocytes but have decreased interactions with immune cell types. Furthermore, given the lack of contrast enhancement in these areas (which suggests an active blood-brain-barrier) and the fact that no more than 20% of cells are cycling at a given time, many of these cells may be completely unaffected by adjuvant chemotherapy, immunotherapy, and radiation therapy. These NPC-/OPC-like tumor cells in the NE region have higher expression of genes that have been identified in regions just beyond gliomas (e.g., *DGKB*, *OPHN1*) (71) and are associated with tumorigenesis (72). Using these and other markers to design specific molecular therapy against these cell types and their molecular drivers is a potential therapeutic strategy. Another

approach may be to limit tumor aggression rather than elimination of all malignant cells. Lower grade gliomas have improved survival, and we observe a relationship between glioma cell types and pathological entity. Specifically, many features of AC-like and MES-like cells are associated with more aggressive glioma, including their upregulated genes in the NE region (*SPARCL1* (73)) as well as hallmark features of high-grade glioma – angiogenesis, ECM breakdown, and immune response. We also find differential regulation of functional pathways between MES-like and OPC-like cellular states. Therefore, a potential therapeutic strategy to slow glioma progression is to maintain a higher proneural (OPC-/NPC-like)-to-mesenchymal (AC-/MES-like) ratio by inhibiting genes and pathways contributing to this transition (16, 32, 74). We find decreased proportions of T cells and decreased interaction with immune cells in NE regions, suggesting that priming these regions for immune response may help improve the efficacy of immunotherapy. Lastly, we identify infiltrating tumor cells as potentially regulating vascular integrity and neural function, suggesting that modulation of vasculature in NE may enhance drug delivery. Overall, we highlight a previously understudied and phenotypically unique population of infiltrating cells that exists outside of the enhancing region on MRI that should be the focus of further clinical and scientific exploration.

Methods

Lead contact and materials availability

Please direct requests for further information and/or resources to Harley Kornblum (hkornblum@mednet.ucla.edu).

MRI-guided biopsy targets in human gliomas

Patients referred to UCLA Neurosurgery for intrinsic supratentorial brain tumors underwent 3 Tesla thin-cut pre-operative MRI (3T Siemens Prisma, Siemens Healthcare, Erlangen, Germany) with and without gadolinium contrast (gadopentetate dimeglumine; Magnevist; Bayer HealthCare Pharmaceuticals) according to the international standardized brain tumor imaging protocol (75) within 1 week of surgery. Images of the following sequences were downloaded: T1 three-dimension magnetization-prepared rapid gradient echo (MP-RAGE) with and without contrast. Using AFNI, a software for analysis and visualization of functional magnetic resonance neuroimages (76), three 5mm x 5mm x 5mm spherical biopsy targets were selected per patient by a multidisciplinary team (neurosurgery, neuroradiology, and neurooncology) based on feasibility and anatomic landmarks in order to minimize surgical inaccuracy from brain shift. Biopsy targets were then transferred to Brainlab Curve (BrainLAB

AG, Munich, Germany), a surgical neuronavigation software, for intraoperative image guidance and tissue acquisition. There was no change to surgical and post-surgical standard of care therapy (77) for all patients. Specimens were immediately fresh frozen for nuclear isolation or paraffin-embedded for immunohistochemistry.

Immunohistochemistry analysis

MRI-targeted biopsy specimens were collected from 17 patients with malignant glioma, yielding 22 specimens from NE regions and 24 from CE regions. Specimens were paraffin-embedded and stained with anti-Ki67 antibody. Image based quantification was done using QuPath (78) to calculate percentage of sample pixels with positive staining. Samples were compared using independent samples t-tests as well as paired samples t-tests in the five patients from whom both CE and NE specimens were acquired.

Single-nucleus RNA sequencing (snRNA-seq) of glioma specimens

Single nuclei were isolated from frozen tumor specimens using iodixanol-based density gradient centrifugation and submitted to UCLA Technology Center for Genomics and Bioinformatics for library preparation and sequencing. Single-nucleus cDNA libraries were generated using the Chromium Single Cell 3' v3 kit (10x Genomics) and sequenced at 600 million reads/library and 2x50 base pairs using the NovaSeq 6000 S2 platform (Illumina). Raw reads were demultiplexed and Cell Ranger (10x Genomics) was used for alignment (human genome GRCh38), filtering, barcode identification, and counting of unique molecular identifiers, resulting in a feature-barcode (i.e., gene-cell) matrix for each biopsy specimen.

SnRNA-seq pre-processing, quality control, and analysis

Feature-barcode matrices were further processed and analyzed individually using the R package Seurat (79–81) except as noted below. Functions were run with default parameters except as specified. Plots were generated with functions native to Seurat or from the visualization package scCustomize (82). For quality control, genes expressed in fewer than 5 nuclei and nuclei expressing fewer than 500 unique genes were both removed. Specimens with a markedly low average number of unique genes expressed per nuclei were removed from the study. Nuclei with mitochondrial transcript content of 5% or greater or ribosomal transcript content of 2% or greater were removed. Counts were normalized and scaled using `SCTransform` (83). For each patient, the datasets from all specimens were then integrated using Seurat's canonical correlation analysis to account for technical variation (80). Dimensional reduction was performed on each patient dataset via principal component analysis (PCA), uniform

manifold approximation and projection (UMAP) embedding, and t-distributed stochastic neighbor embedding (t-SNE). Clustering was performed in each patient dataset using Seurat's default graph-based clustering, and low dimensional plots were generated using the `DimPlot` function. Malignant cells and subclones were identified using a custom tool that combines marker expression patterns, hierarchical relationships across unbiased clusters, and an iterative sequence of single-cell copy number alteration (CNA) inference analyses to address problematic cells (i.e., incorrect cluster assignment, noisy or unclear CNA profiles) (see Supplemental Methods). Malignant cells were grouped by cellular state (AC-, MES-, NPC-, or OPC-like) and by cycling status using single-cell gene module scores, as reported by Neftel et al. (13) and their respective pathway enrichment profiles were identified with enrichR (84–86). Non-malignant cell types were identified based on marker expression profiles (using a modified tool for improved visualization of marker expression across clusters) and hierarchical clustering, yielding astrocytes, oligodendrocytes, excitatory neurons, interneurons, endothelial cells, T cells, tumor-associated macrophages, and microglia. The integrated dataset for each patient was then split into malignant and non-malignant datasets, which were processed again as above then integrated across patients. The two resulting datasets (malignant cells from all patients, non-malignant cells from all patients) were then prepared for further analysis by dimensional reduction and Seurat clustering as above. Differentially expressed genes (DEGs) were identified using the Seurat functions `FindMarkers` (within-group) and `FindConservedMarkers` (shared) and visualized using `EnhancedVolcano`. Genes expressed in at least 5% of cells were included; significance was defined as a 10% change in expression with $p<0.05$ (adjusted p-value for `FindMarkers`, combined p-value for `FindConservedMarkers`). Gene set enrichment analysis (GSEA) was performed on DEGs ranked by fold change using the fgsea package (87) with a combination of Gene Ontology Biological Pathways, Canonical Pathways, Oncogenic Pathways, and Transcription Factor Targets (42). Details for the above and additional analyses (quantification of heterogeneity, identification of putative glioma stem cells, cell-cell communication analysis) are further discussed in Supplemental Methods.

Estimating extent of tumor burden

Cell type abundances from single-cell sequencing data were used to calculate the tumor cell burden at different biopsy sites. Tumor cell number was normalized by the non-tumor oligodendrocyte number to control for total cells sequenced, which varied per sample. Segmentations of contrast-enhancing lesion of tumor were calculated using

previously described methods (88). Using AFNI (76), this segmentation was minimized to obtain an ROI at the volumetric center of the lesion. The distance between the prospective biopsy ROI and this center of lesion ROI was calculated. The tumor:oligodendrocyte ratio was plotted against this distance. A quadratic model was implemented (89):

$$x = \frac{-b \pm \sqrt{b^2 - 4ac}}{2a}$$

and x solved to identify the Y asymptote as the predicted distance from center when cell ratio approaches 0. A spherical heatmap ROI with radius r equal to this distance was created and overlayed on T1 with contrast images.

$$V = \frac{4}{3}\pi r^3$$

Statistics

Statistical analysis was carried out in GraphPad Prism (GraphPad Software, San Diego, CA, USA). Independent and paired t-tests and chi-square tests were used to evaluate differences in tumor and non-tumor cell quantities, cellular states, cell cycling proportions and % positive Ki-67. Differential gene expression and pathway enrichment analyses underwent correction for multiple comparisons using the native functionality of the Seurat and fgsea packages, respectively. Significance was defined using an alpha level of 0.05 except as noted in figures.

Study Approval

This study was approved by the UCLA IRB #10-000655 and #14-001261. All patients provided informed consent for all medical and surgical procedures and involvement in research studies.

Data availability

Sequencing data will be made available to the public through a GEO submission. Processed data objects and custom scripts for downstream analyses and figure generation will be shared through a GitHub repository at the time of publication (and is available upon request for the editorial process).

Acknowledgements

This work was supported by the Dr. Miriam and Sheldon G. Adelson Medical Research Foundation (HIK, RK, SAG); NIH grants P50 CA211015 (HIK, BE, DG, WY, LL), R01 NS121617 (HIK), and F31 MH122205 (KKT); the Broad Stem Cell Research Center (KSP, SDM); and the UC President's Postdoctoral Fellowship Program (AGA).

Author Contributions

KP: study conception; acquiring data; analyzing data; writing/revising manuscript

KT: acquiring data; analyzing data; figure generation; writing/revising manuscript

RK: analyzing data; figure generation

AA: analyzing data; writing/revising manuscript

SM: analyzing data; writing/revising manuscript

AH: acquiring data; analyzing data

VS: analyzing data; study supervision

LL: acquiring data; revising manuscript, study supervision

AW: acquiring data; revising manuscript, study supervision

WY: acquiring data; revising manuscript, study supervision

DG: acquiring data; revising manuscript, study supervision

IN: revising manuscript, study supervision

SG: revising manuscript, study supervision

RE: study conception; acquiring data; revising manuscript, study supervision

BE: study conception; acquiring data; analyzing data; revising manuscript, study supervision

HK: study conception; acquiring data; analyzing data; writing/revising manuscript, study supervision

First authorship order was determined by corresponding author by individual contribution

References

1. Brown TJ et al. Association of the Extent of Resection With Survival in Glioblastoma: A Systematic Review and Meta-analysis. *JAMA Oncol* 2016;2(11):1460–1469.

2. Marko NF et al. Extent of resection of glioblastoma revisited: personalized survival modeling facilitates more accurate survival prediction and supports a maximum-safe-resection approach to surgery. *J Clin Oncol* 2014;32(8):774–782.

3. Wen PY, Kesari S. Malignant gliomas in adults. *N. Engl. J. Med.* 2008;359(5):492–507.

4. Sanai N, Polley M-Y, McDermott MW, Parsa AT, Berger MS. An extent of resection threshold for newly diagnosed glioblastomas. *J. Neurosurg.* 2011;115(1):3–8.

5. Ellingson BM et al. Validation of postoperative residual contrast-enhancing tumor volume as an independent prognostic factor for overall survival in newly diagnosed glioblastoma. *Neuro Oncol* 2018;20(9):1240–1250.

6. Bette S et al. Retrospective Analysis of Radiological Recurrence Patterns in Glioblastoma, Their Prognostic Value And Association to Postoperative Infarct Volume. *Sci Rep* 2018;8(1):4561.

7. Erdem-Eraslan L et al. Identification of Patients with Recurrent Glioblastoma Who May Benefit from Combined Bevacizumab and CCNU Therapy: A Report from the BELOB Trial. *Cancer Res* 2016;76(3):525–534.

8. Taal W et al. Single-agent bevacizumab or lomustine versus a combination of bevacizumab plus lomustine in patients with recurrent glioblastoma (BELOB trial): a randomised controlled phase 2 trial. *Lancet Oncol.* 2014;15(9):943–953.

9. Brandes AA et al. AVAREG: a phase II, randomized, noncomparative study of fotemustine or bevacizumab for patients with recurrent glioblastoma. *Neuro Oncol* 2016;18(9):1304–1312.

10. Cloughesy TF et al. Neoadjuvant anti-PD-1 immunotherapy promotes a survival benefit with intratumoral and systemic immune responses in recurrent glioblastoma. *Nat Med* 2019;25(3):477–486.

11. Patel AP et al. Single-cell RNA-seq highlights intratumoral heterogeneity in primary glioblastoma. *Science* 2014;344(6190):1396–1401.

12. Venteicher AS et al. Decoupling genetics, lineages, and microenvironment in IDH-mutant gliomas by single-cell RNA-seq. *Science* 2017;355(6332). doi:10.1126/science.aai8478

13. Neftel C et al. An Integrative Model of Cellular States, Plasticity, and Genetics for Glioblastoma. *Cell* 2019;178(4):835-849.e21.

14. Tirosh I et al. Single-cell RNA-seq supports a developmental hierarchy in human oligodendroglioma. *Nature* 2016;539(7628):309–313.

15. Weng Q et al. Single-Cell Transcriptomics Uncovers Glial Progenitor Diversity and Cell Fate Determinants during Development and Gliomagenesis. *Cell Stem Cell* 2019;24(5):707-723.e8.

16. Wang L et al. The Phenotypes of Proliferating Glioblastoma Cells Reside on a Single Axis of Variation. *Cancer Discov* 2019;9(12):1708–1719.

17. Lan X et al. Fate mapping of human glioblastoma reveals an invariant stem cell hierarchy. *Nature* 2017;549(7671):227–232.

18. Abdelfattah N et al. Single-cell analysis of human glioma and immune cells identifies S100A4 as an immunotherapy target. *Nat Commun* 2022;13(1):767.

19. Darmanis S et al. Single-Cell RNA-Seq Analysis of Infiltrating Neoplastic Cells at the Migrating Front of Human Glioblastoma. *Cell Rep* 2017;21(5):1399–1410.

20. Louis DN et al. The 2021 WHO Classification of Tumors of the Central Nervous System: a summary. *Neuro Oncol* 2021;23(8):1231–1251.

21. Couturier CP et al. Single-cell RNA-seq reveals that glioblastoma recapitulates a normal neurodevelopmental hierarchy. *Nat Commun* 2020;11(1):3406.

22. Squair JW, Skinnider MA, Gautier M, Foster LJ, Courtine G. Prioritization of cell types responsive to biological perturbations in single-cell data with Augur. *Nat Protoc* 2021;16(8):3836–3873.

23. Schaub C et al. Tumor growth patterns of MGMT-non-methylated glioblastoma in the randomized GLARIUS trial. *J. Cancer Res. Clin. Oncol.* 2018;144(8):1581–1589.

24. Jin X et al. Targeting glioma stem cells through combined BMI1 and EZH2 inhibition. *Nat Med* 2017;23(11):1352–1361.

25. Eberhart CG, Bar EE. Spatial enrichment of cellular states in glioblastoma. *Acta Neuropathol* 2020;140(1):85–87.

26. Minata M et al. Phenotypic Plasticity of Invasive Edge Glioma Stem-like Cells in Response to Ionizing Radiation. *Cell Rep* 2019;26(7):1893-1905.e7.

27. El Ayachi I et al. KIAA0510, the 3'-untranslated region of the tenascin-R gene, and tenascin-R are overexpressed in pilocytic astrocytomas. *Neuropathol Appl Neurobiol* 2010;36(5):399–410.

28. Ducray F et al. Anaplastic oligodendrogliomas with 1p19q codeletion have a proneural gene expression profile. *Mol Cancer* 2008;7:41.

29. Lin K et al. TMEFF2 is a PDGF-AA binding protein with methylation-associated gene silencing in multiple cancer types including glioma. *PLoS One* 2011;6(4):e18608.

30. Magne N et al. PAK3 is a key signature gene of the glioma proneural subtype and affects its proliferation, differentiation and growth. *Cell Oncol (Dordr)* 2021;44(6):1257–1271.

31. Colin C et al. Identification of genes differentially expressed in glioblastoma versus pilocytic astrocytoma using Suppression Subtractive Hybridization. *Oncogene* 2006;25(19):2818–2826.

32. Feng P, Li Z, Li Y, Zhang Y, Miao X. Characterization of Different Subtypes of Immune Cell Infiltration in Glioblastoma to Aid Immunotherapy. *Front Immunol* 2022;13:799509.

33. Pirmoradi L, Seyfizadeh N, Ghavami S, Zeki AA, Shojaei S. Targeting cholesterol metabolism in glioblastoma: a new therapeutic approach in cancer therapy. *J Investig Med* 2019;67(4):715–719.

34. Tateishi K et al. Myc-Driven Glycolysis Is a Therapeutic Target in Glioblastoma. *Clin Cancer Res* 2016;22(17):4452–4465.

35. Mooney KL et al. The role of CD44 in glioblastoma multiforme. *J Clin Neurosci* 2016;34:1–5.

36. Wei J et al. Osteopontin mediates glioblastoma-associated macrophage infiltration and is a potential therapeutic target. *J Clin Invest* 2019;129(1):137–149.

37. Dong C, Zhang J, Fang S, Liu F. IGFBP5 increases cell invasion and inhibits cell proliferation by EMT and Akt signaling pathway in Glioblastoma multiforme cells. *Cell Div* 2020;15:4.

38. Kang SS et al. Caffeine-mediated inhibition of calcium release channel inositol 1,4,5-trisphosphate receptor subtype 3 blocks glioblastoma invasion and extends survival. *Cancer Res* 2010;70(3):1173–1183.

39. Angel I, Pilo Kerman O, Rousso-Noori L, Friedmann-Morvinski D. Tenascin C promotes cancer cell plasticity in mesenchymal glioblastoma. *Oncogene* 2020;39(46):6990–7004.

40. Pen A, Moreno MJ, Durocher Y, Deb-Rinker P, Stanimirovic DB. Glioblastoma-secreted factors induce IGFBP7 and angiogenesis by modulating Smad-2-dependent TGF-beta signaling. *Oncogene* 2008;27(54):6834–6844.

41. Subramanian A et al. Gene set enrichment analysis: a knowledge-based approach for interpreting genome-wide expression profiles. *Proc Natl Acad Sci U S A* 2005;102(43):15545–15550.

42. Liberzon A et al. Molecular signatures database (MSigDB) 3.0. *Bioinformatics* 2011;27(12):1739–1740.

43. Guo S-W, Zheng Y, Lu Y, Liu X, Geng J-G. Slit2 overexpression results in increased microvessel density and lesion size in mice with induced endometriosis. *Reprod Sci* 2013;20(3):285–298.

44. Wang B et al. Induction of tumor angiogenesis by Slit-Robo signaling and inhibition of cancer growth by blocking Robo activity. *Cancer Cell* 2003;4(1):19–29.

45. Wang L-J et al. Targeting Slit-Roundabout signaling inhibits tumor angiogenesis in chemical-induced squamous cell carcinogenesis. *Cancer Sci* 2008;99(3):510–517.

46. Li S et al. Slit2 Promotes Angiogenic Activity Via the Robo1-VEGFR2-ERK1/2 Pathway in Both In Vivo and In Vitro Studies. *Invest Ophthalmol Vis Sci* 2015;56(9):5210–5217.

47. Suvà ML, Tirosh I. The Glioma Stem Cell Model in the Era of Single-Cell Genomics. *Cancer Cell* 2020;37(5):630–636.

48. Bhaduri A et al. Outer Radial Glia-like Cancer Stem Cells Contribute to Heterogeneity of Glioblastoma. *Cell Stem Cell* 2020;26(1):48-63.e6.

49. Xie XP et al. Quiescent human glioblastoma cancer stem cells drive tumor initiation, expansion, and recurrence following chemotherapy. *Dev Cell* 2022;57(1):32-46.e8.

50. Suvà ML et al. Reconstructing and reprogramming the tumor-propagating potential of glioblastoma stem-like cells. *Cell* 2014;157(3):580–594.

51. Antonica F et al. A slow-cycling/quiescent cells subpopulation is involved in glioma invasiveness. *Nat Commun* 2022;13(1):4767.

52. Tong M, Jun T, Nie Y, Hao J, Fan D. The Role of the Slit/Robo Signaling Pathway. *J Cancer* 2019;10(12):2694–2705.

53. Treiber JM et al. Molecular physiology of contrast enhancement in glioblastomas: An analysis of The Cancer Imaging Archive (TCIA). *J Clin Neurosci* [published online ahead of print: June 19, 2018]; doi:10.1016/j.jocn.2018.06.018

54. Caspani EM, Crossley PH, Redondo-Garcia C, Martinez S. Glioblastoma: a pathogenic crosstalk between tumor cells and pericytes. *PLoS One* 2014;9(7):e101402.

55. Venkatesh HS et al. Neuronal Activity Promotes Glioma Growth through Neuroligin-3 Secretion. *Cell* 2015;161(4):803–816.

56. Venkatesh HS et al. Targeting neuronal activity-regulated neuroligin-3 dependency in high-grade glioma. *Nature* 2017;549(7673):533–537.

57. Venkatesh HS et al. Electrical and synaptic integration of glioma into neural circuits. *Nature* 2019;573(7775):539–545.

58. Jin S et al. Inference and analysis of cell-cell communication using CellChat. *Nat Commun* 2021;12(1):1088.

59. Manini I et al. Semaphorin-7A on Exosomes: A Promigratory Signal in the Glioma Microenvironment. *Cancers (Basel)* 2019;11(6):758.

60. Zhang DF, Li XG, Su LJ, Meng QL. Expression of activin A and follistatin in glioblastoma and their effects on U87 in vitro. *J Int Med Res* 2010;38(4):1343–1353.

61. Saraswathula A et al. Serum elevation of B lymphocyte stimulator does not increase regulatory B cells in glioblastoma patients undergoing immunotherapy. *Cancer Immunol Immunother* 2016;65(2):205–211.

62. Walker PR, Migliorini D. The CD40/CD40L axis in glioma progression and therapy. *Neuro Oncol* 2015;17(11):1428–1430.

63. Han M et al. Comprehensive characterization of TNFSF14/LIGHT with implications in prognosis and immunotherapy of human gliomas. *Front Immunol* 2022;13:1025286.

64. Sloan KE, Stewart JK, Treloar AF, Matthews RT, Jay DG. CD155/PVR enhances glioma cell dispersal by regulating adhesion signaling and focal adhesion dynamics. *Cancer Res* 2005;65(23):10930–10937.

65. Xu C, Zhu S, Wu M, Han W, Yu Y. Functional receptors and intracellular signal pathways of midkine (MK) and pleiotrophin (PTN). *Biol Pharm Bull* 2014;37(4):511–520.

66. Ku M-C et al. GDNF mediates glioblastoma-induced microglia attraction but not astrogliosis. *Acta Neuropathol* 2013;125(4):609–620.

67. Gill BJ et al. MRI-localized biopsies reveal subtype-specific differences in molecular and cellular composition at the margins of glioblastoma. *Proc. Natl. Acad. Sci. U.S.A.* 2014;111(34):12550–12555.

68. Mao X-G et al. CDH5 is specifically activated in glioblastoma stemlike cells and contributes to vasculogenic mimicry induced by hypoxia. *Neuro Oncol* 2013;15(7):865–879.

69. Khong A, Brown MD, Vivian JB, Robinson BWS, Currie AJ. Agonistic anti-CD40 antibody therapy is effective against postoperative cancer recurrence and metastasis in a murine tumor model. *J Immunother* 2013;36(7):365–372.

70. Chonan M et al. CD40/CD40L expression correlates with the survival of patients with glioblastomas and an augmentation in CD40 signaling enhances the efficacy of vaccinations against glioma models. *Neuro Oncol* 2015;17(11):1453–1462.

71. Ljubimova JY et al. Gene expression abnormalities in human glial tumors identified by gene array. *Int J Oncol* 2001;18(2):287–295.

72. Yang J et al. Circular RNA DGKB Promotes the Progression of Neuroblastoma by Targeting miR-873/GLI1 Axis. *Front Oncol* 2020;10:1104.

73. Gagliardi F et al. Enhanced SPARCL1 expression in cancer stem cells improves preclinical modeling of glioblastoma by promoting both tumor infiltration and angiogenesis. *Neurobiol Dis* 2020;134:104705.

74. Chen Z et al. FOSL1 promotes proneural-to-mesenchymal transition of glioblastoma stem cells via UBC9/CYLD/NF-κB axis. *Mol Ther* 2022;30(7):2568–2583.

75. Ellingson BM et al. Consensus recommendations for a standardized Brain Tumor Imaging Protocol in clinical trials. *Neuro-oncology* 2015;17(9):1188–1198.

76. Cox RW. AFNI: software for analysis and visualization of functional magnetic resonance neuroimages. *Comput. Biomed. Res.* 1996;29(3):162–173.

77. Stupp R et al. Radiotherapy plus concomitant and adjuvant temozolomide for glioblastoma. *N. Engl. J. Med.* 2005;352(10):987–996.

78. Bankhead P et al. QuPath: Open source software for digital pathology image analysis. *Sci Rep* 2017;7(1):16878.

79. Heinemann J. Cluster Analysis of Untargeted Metabolomic Experiments. *Methods Mol Biol* 2019;1859:275–285.

80. Stuart T et al. Comprehensive Integration of Single-Cell Data. *Cell* 2019;177(7):1888-1902.e21.

81. Hao Y et al. Integrated analysis of multimodal single-cell data. *Cell* 2021;184(13):3573-3587.e29.

82. Marsh S. scCustomize: Custom Visualizations & Functions for Streamlined Analysis of Single Cell Sequencing [Internet]2023;https://samuel-marsh.github.io/scCustomize/. cited

83. Hafemeister C, Satija R. Normalization and variance stabilization of single-cell RNA-seq data using regularized negative binomial regression. *Genome Biol* 2019;20(1):296.

84. Chen EY et al. Enrichr: interactive and collaborative HTML5 gene list enrichment analysis tool. *BMC Bioinformatics* 2013;14:128.

85. Kuleshov MV et al. Enrichr: a comprehensive gene set enrichment analysis web server 2016 update. *Nucleic Acids Res* 2016;44(W1):W90-97.

86. Xie Z et al. Gene Set Knowledge Discovery with Enrichr. *Curr Protoc* 2021;1(3):e90.

87. Korotkevich G, Sukhov V, Sergushichev A. Fast gene set enrichment analysis [Internet]2019;bioRxiv. doi:10.1101/060012, http://biorxiv.org/content/early/2016/06/20/060012. cited

88. Ellingson BM et al. Volumetric response quantified using T1 subtraction predicts long-term survival benefit from cabozantinib monotherapy in recurrent glioblastoma. *Neuro Oncol* 2018;20(10):1411–1418.

89. Williams MV, Denekamp J, Fowler JF. A review of alpha/beta ratios for experimental tumors: implications for clinical studies of altered fractionation. *Int J Radiat Oncol Biol Phys* 1985;11(1):87–96.

Figure 1. Single-nucleus RNA-sequencing analysis of MRI-guided glioma biopsy targets

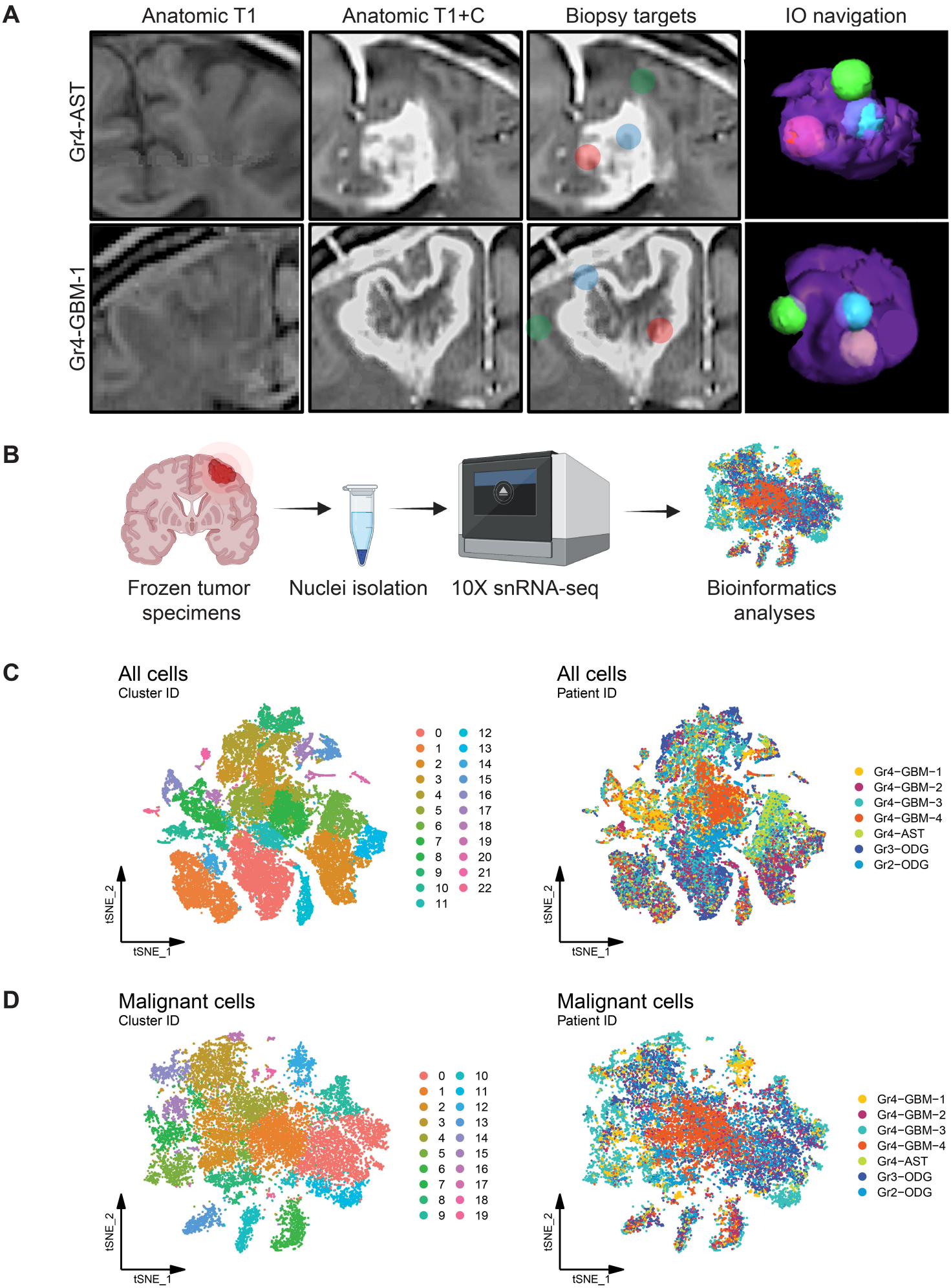

Figure 2. Recapitulation of established malignant cellular states in recurrent glioma

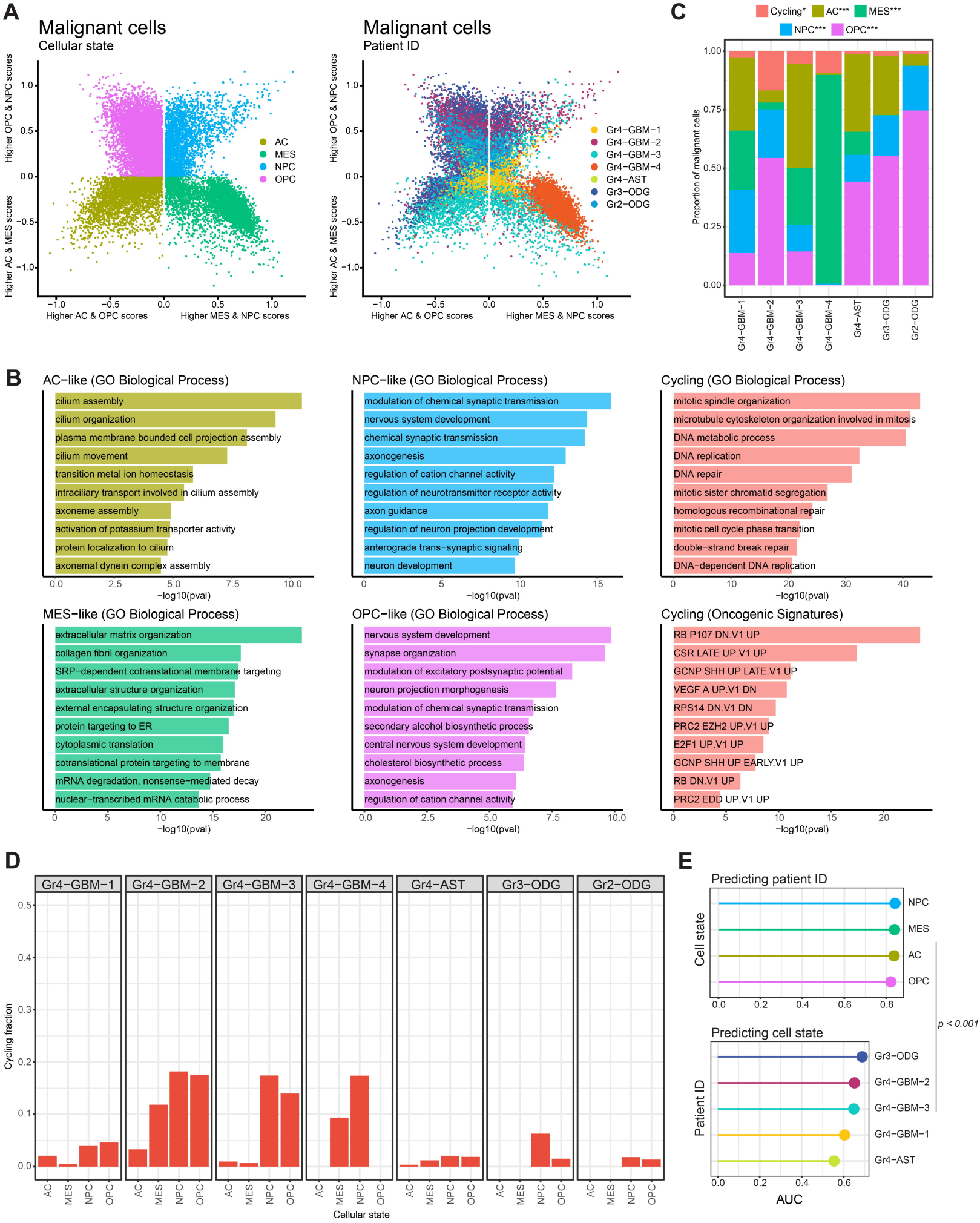

Figure 3. Characterizing tumor burden and composition in the non-enhancing region

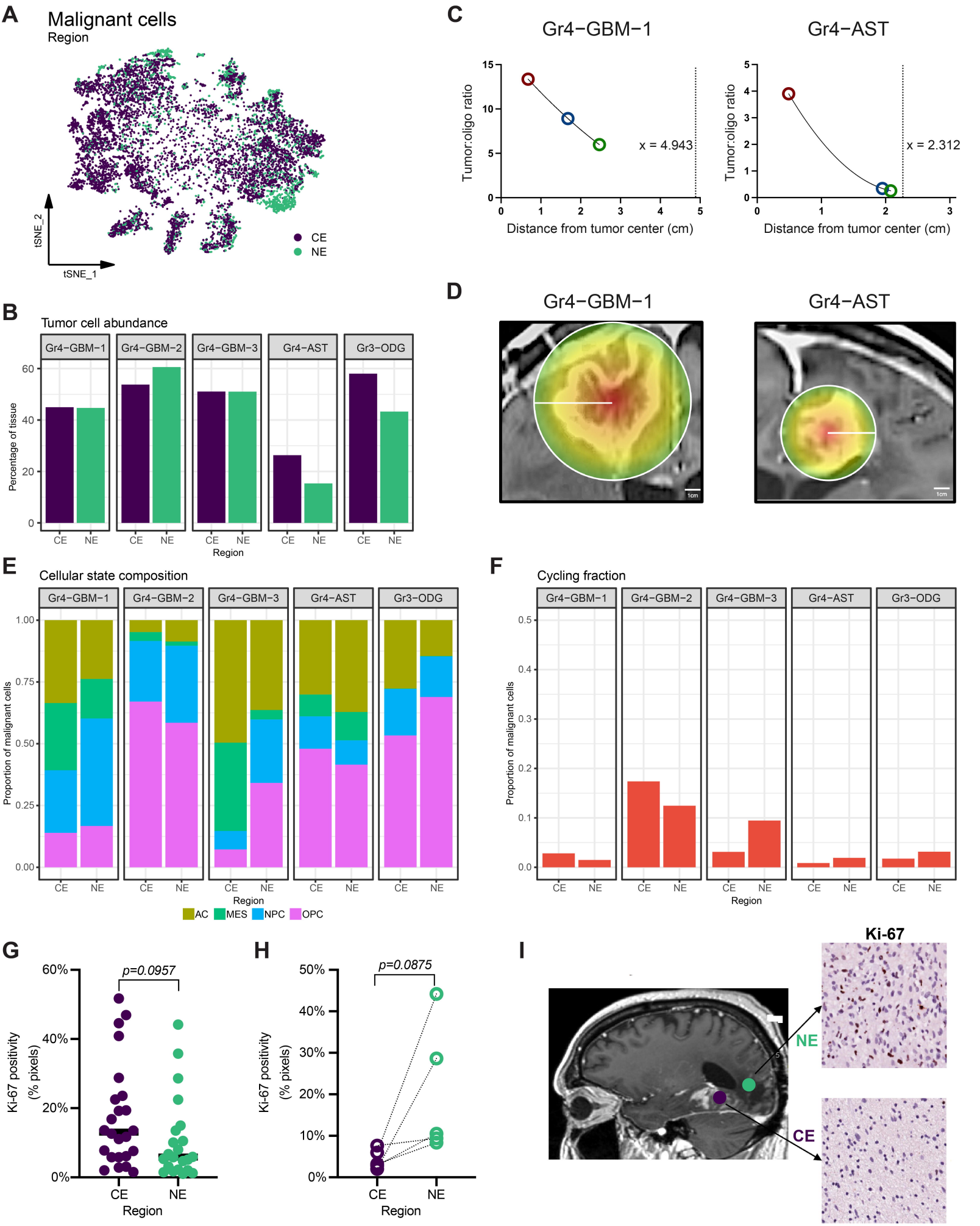

Figure 4. Region-specific molecular features of malignant cells in high-grade glioma

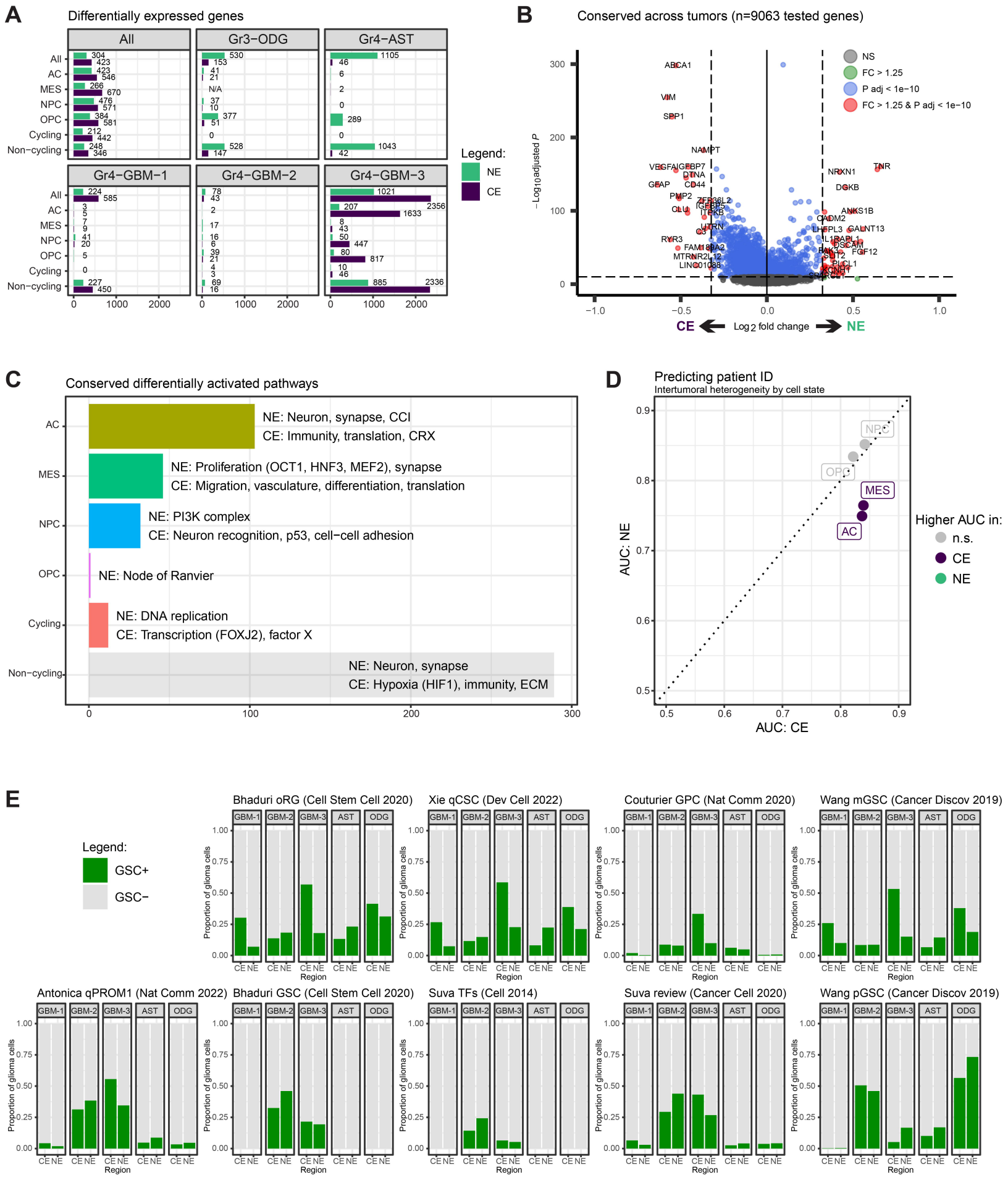

Figure 5. Altered non-malignant cell microenvironment in NE region of high-grade gliomas

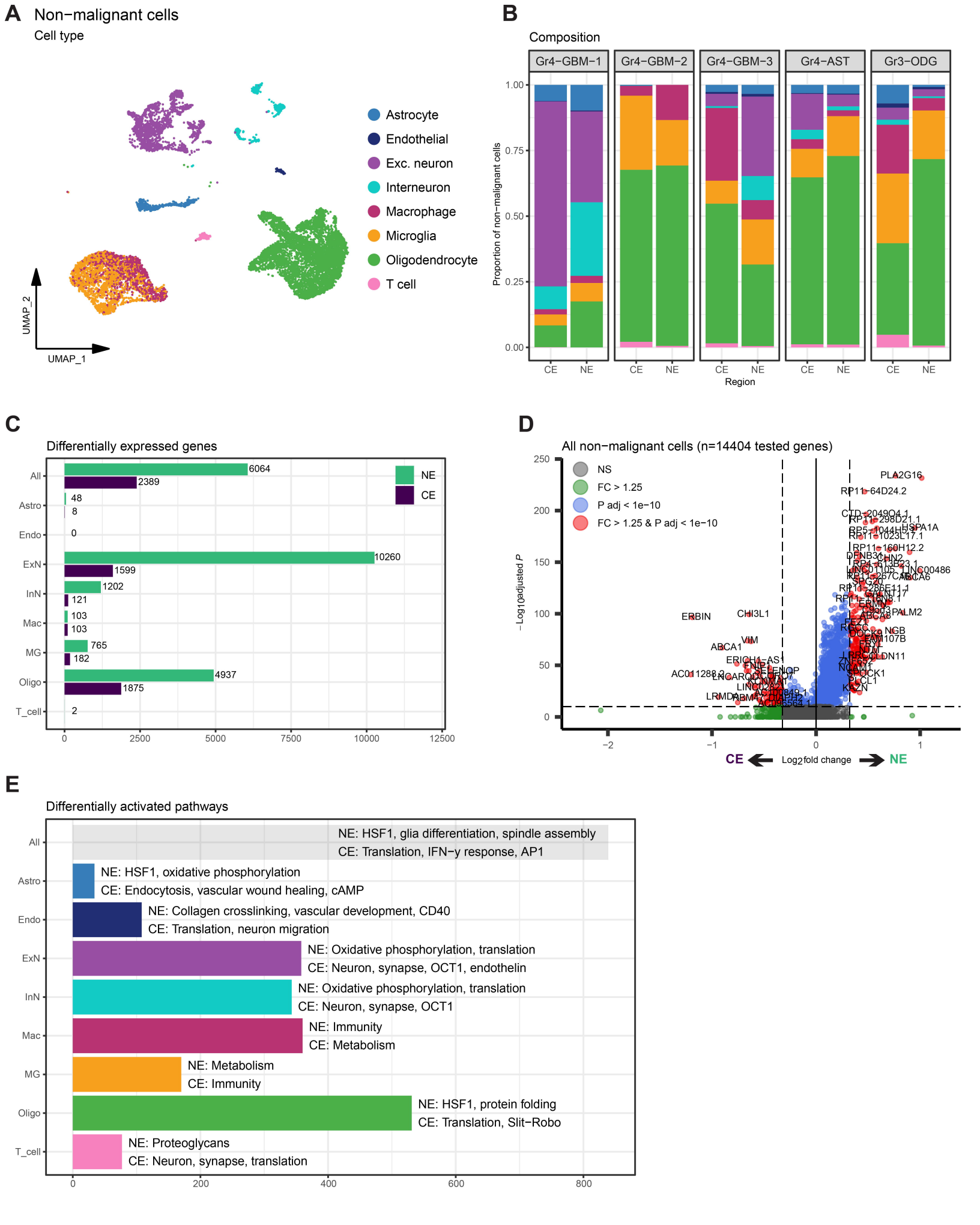

Figure 6. Regional differences in cell-cell interaction strength at the cell type level

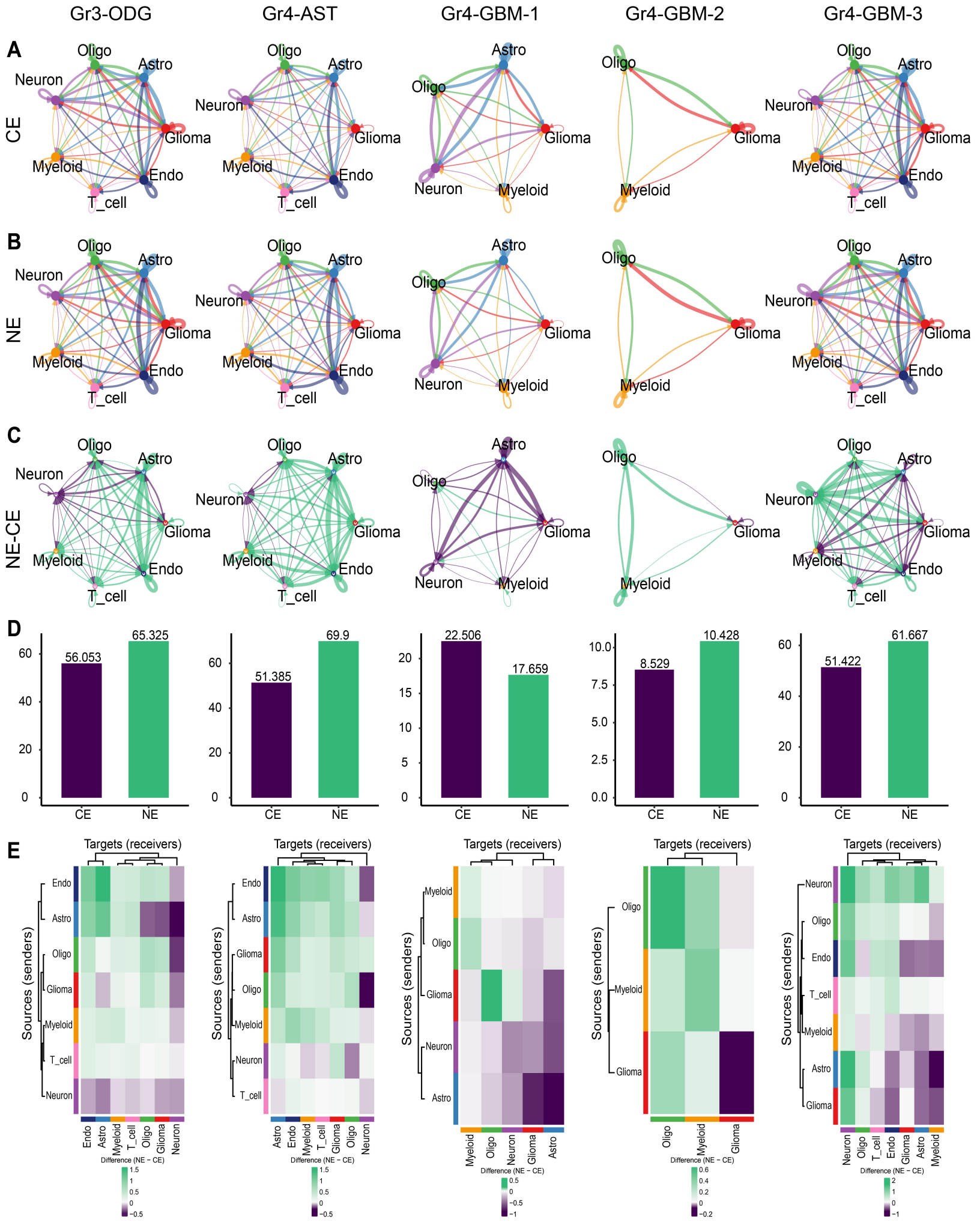
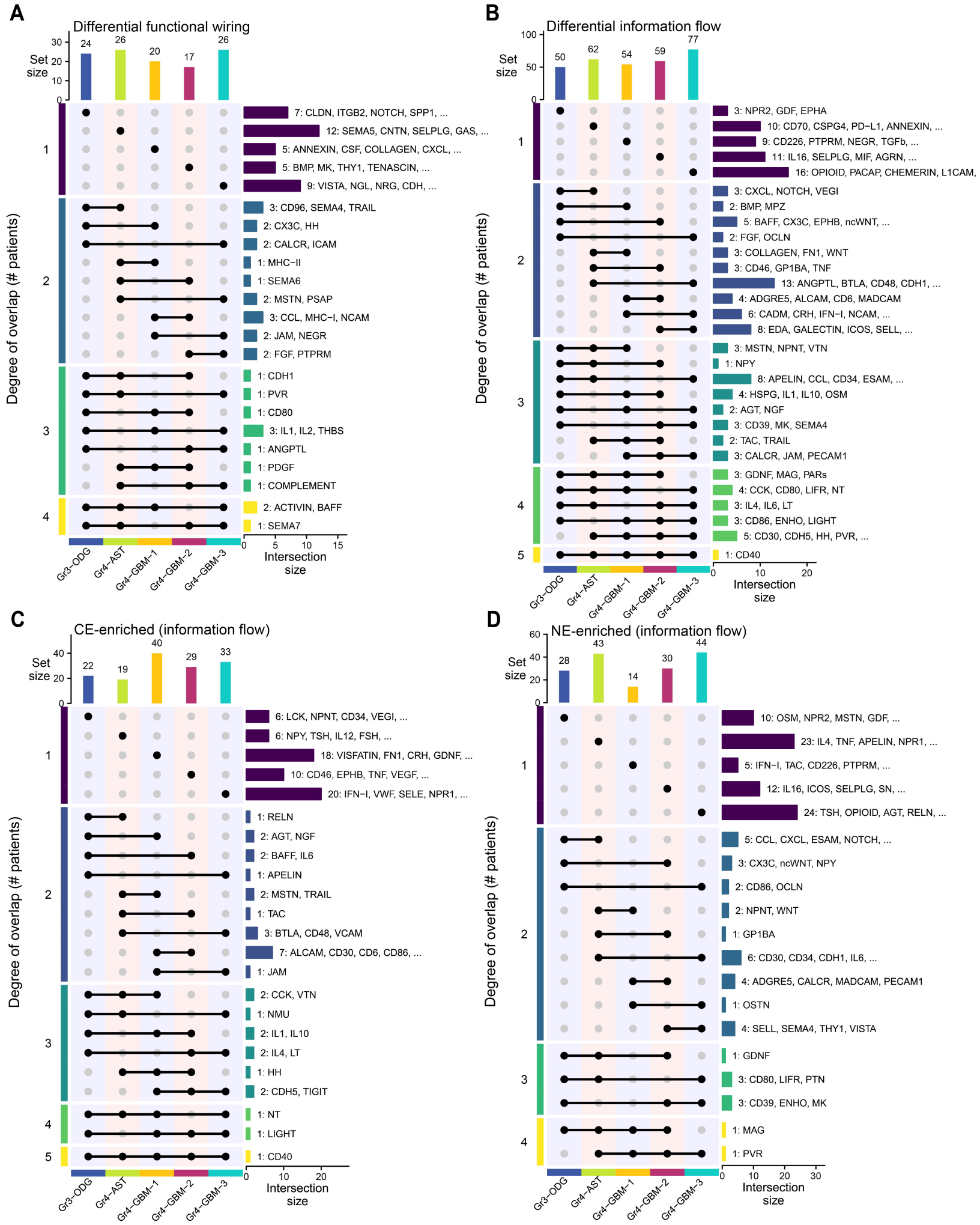
Figure 7. Shared regional differences in communication network wiring and information flow